


RESEARCH

Open Access



# Effect and underlying mechanism of a photochemotherapy dual-function nanodrug delivery system for head and neck squamous cell carcinoma

Qian Lin<sup>1†</sup>, Hui-Min Liu<sup>2†</sup>, Li-Zhi Wu<sup>1</sup>, Dong-Dong Yu<sup>3</sup>, Cheng-Yu Hua<sup>1</sup>, You Zou<sup>1</sup>, Wo-Er Jiao<sup>1</sup>, Xiang-Pan Li<sup>3\*</sup> and Shi-Ming Chen<sup>1\*</sup> 

## Abstract

**Background** The novel nanomaterials PNA-TN (PN) and PNA-TN-Dox (PND) have been shown to have strong inhibitory effects on breast cancer; however, it is unclear whether PN and PND have anti-head and neck squamous cell carcinoma (HNSCC) activity, and their potential mechanisms of activity are unknown. So, our study aims to explore the therapeutic effects of PN and PND on HNSCC and their possible mechanisms.

**Methods** We used a series of phenotypic research to evaluate the effects of PN + Laser (L) and PND + L on the biological function of HNSCC cells in vitro and in vivo. We subsequently used mechanism research to examine changes in mRNA and protein expression related to apoptosis, epithelial–mesenchymal transition (EMT), and the JNK signalling pathway.

**Results** Our study revealed that PN and PND have strong inhibitory effects on HNSCC cells both in vitro and in vivo. In vitro, PN and PND significantly inhibited the proliferation, migration, invasion and EMT ability of HNSCC cells and promoted apoptosis; the inhibitory effect in the PND + L group was significantly greater than that in the PN + L group. In vivo, both treatments led to significant reductions in tumour volume and weight. Notably, the tumour volume and weight in the PND + L group were significantly lower than those in the PN + L group. Mechanism research confirmed that PN + L activated the expression of apoptosis-related proteins and inhibited the expression of EMT-related proteins via the JNK pathway. Furthermore, the anti-HNSCC effect of PN + L was blocked after the use of a JNK pathway inhibitor.

<sup>†</sup>Qian Lin and Hui-Min Liu contributed equally to this work.

\*Correspondence:

Xiang-Pan Li  
rm001227@whu.edu.cn  
Shi-Ming Chen  
shimingchen0468@163.com

Full list of author information is available at the end of the article



© The Author(s) 2024. **Open Access** This article is licensed under a Creative Commons Attribution-NonCommercial-NoDerivatives 4.0 International License, which permits any non-commercial use, sharing, distribution and reproduction in any medium or format, as long as you give appropriate credit to the original author(s) and the source, provide a link to the Creative Commons licence, and indicate if you modified the licensed material. You do not have permission under this licence to share adapted material derived from this article or parts of it. The images or other third party material in this article are included in the article's Creative Commons licence, unless indicated otherwise in a credit line to the material. If material is not included in the article's Creative Commons licence and your intended use is not permitted by statutory regulation or exceeds the permitted use, you will need to obtain permission directly from the copyright holder. To view a copy of this licence, visit <http://creativecommons.org/licenses/by-nc-nd/4.0/>.

**Conclusion** Treatment with PN+L or PND+L significantly inhibited the malignant progress of HNSCC cells, and the therapeutic effect of PND+L was significantly stronger than that of PN+L. The JNK signalling pathway is a key mechanism by which PN exerts its anti-HNSCC activity.

**Keywords** Head and neck squamous cell carcinoma, Nanomedicine, Photochemotherapy, JNK signalling pathway

## Introduction

Head and neck squamous cell carcinoma (HNSCC) originates from the mucosal epithelium of the oral cavity, pharynx, and larynx and is the most common malignant tumour in the head and neck region [1]. In 2023, over 400,000 people worldwide were diagnosed with HNSCC, with a recurrence rate exceeding 50% within two years of treatment [2]. The incidence of HNSCC, particularly oropharyngeal cancer, is influenced by geographical factors, is often associated with smoking and excessive alcohol consumption, and is strongly associated with the HPV-16 subtype [3]. The main treatment methods for HNSCC include surgery, radiotherapy, and chemotherapy. For patients with small primary cancers without lymph node involvement or involving only a single lymph node, the cure rate can exceed 80% through single-modality interventions such as surgical resection or radiotherapy [4]. However, for patients with advanced HNSCC, concurrent chemoradiation therapy (CCRT) is the preferred treatment method [5], and immune checkpoint inhibitors (ICIs) have been effective for patients with recurrence or metastasis [6]. Although these clinical trial results have shown an improvement in the overall survival rate of patients, some patients are not sensitive to these treatments, resulting in no significant increase in the 5-year survival rate of HNSCC patients over the past 30 years [7, 8]. Therefore, the development of new efficient drug treatments for HNSCC is highly important.

Compared with traditional methods such as surgery, radiotherapy, and chemotherapy, phototherapy has unique advantages such as noninvasiveness, high spatial and temporal controllability, minimal side effects, and low drug resistance [9]. Among them, photothermal therapy (PTT), as a supplement to traditional radiochemotherapy, is receiving increasing attention [10]. This treatment method can effectively convert near-infrared (NIR) radiation into thermal energy by activating photothermal converters, inducing tumour cell apoptosis through thermal ablation [11]. Although PTT is usually not sufficient to completely eradicate tumours, its combination with chemotherapy has been more effective than the use of either therapy alone [12].

In recent years, nanomaterials have been widely developed for tumour treatment, drug delivery, and disease imaging [12–14], among which materials and nanoparticles related to aggregation-induced emission (AIE) have attracted widespread attention because of their multifunctional characteristics [15]. Many studies have shown

that AIE-based nanomaterials have broad prospects in the fields of luminescent materials, sensors, bioimaging, drug delivery, and theranostics [14, 16, 17].

C-Jun N-terminal kinases (JNKs) and their variants JNK1, JNK2, and JNK3 constitute a subfamily of mitogen-activated protein kinases (MAPKs) [18]. The JNK signalling pathway affects a series of cellular activities, including proliferation, differentiation, apoptosis, angiogenesis, and migration [19], by integrating a wide range of intracellular signalling pathways to regulate gene expression and the homeostasis of macromolecules (including mRNAs and proteins) [20]. In recent years, numerous studies have shown that JNK plays an important role in cell apoptosis and tumour suppression [21–24]. The JNK signalling pathway directly targets mitochondria through the phosphorylation of Bad and Bim to activate Bax and/or Bak, and these proapoptotic proteins can also inhibit the activity of antiapoptotic proteins such as Bcl-2 and Bcl-xL, thus promoting cell apoptosis [25]. In addition, JNK signal transduction plays an important role in the regulation of cell migration and tumour invasion [26].

In this study, we demonstrate that AIE-based functional nanogels, effectively integrating the AIE photothermal contrast agent and the traditional chemotherapeutic drug Doxorubicin (Dox) to achieve precise synergistic photochemotherapy [27]. Our results reveal that PNA-TN (PN) and PNA-TN-Dox (PND) combined with NIR irradiation can significantly inhibit the proliferation and EMT process of HNSCC cells, inducing cell apoptosis. Mechanistically, PN+Laser (L) effectively activated the JNK signalling pathway and suppressed the malignant phenotype of HNSCC.

## Materials and methods

### Cell culture and reagents

Human tongue squamous cell carcinoma Cal27 cells and human laryngeal squamous cell carcinoma Tu686 cells, normal oral epithelial keratinocytes HOK cells were purchased from the American Type Culture Collection (ATCC). The culture conditions for all the cells were as follows: Dulbecco's modified Eagle medium (DMEM; Servicebio, Wuhan, China), 10% fetal bovine serum (FBS; Servicebio, Wuhan, China), and 1% penicillin-streptomycin solution (Biosharp, Hefei, China). The incubator environment was maintained at 37 °C and 5% CO<sub>2</sub>. All experiments were conducted on cells in the logarithmic growth phase and were repeated at least three times.

The materials PN and PND used in this study were kindly provided by the research group of Professor Ben Zhong Tang from the Chinese University of Hong Kong, and the specific synthesis scheme can be found in previous reports [27]. The synthesis process is roughly as follows: First, a thermo/pH-responsive polymer backbone with thermo-responsive and pH-responsive segments was synthesized through precipitation polymerization, namely poly (N-isopropylacrylamide-co-acrylic acid) nanogels (abbreviated as PNA). Then, TPA-NDTA (referred to as TN) was encapsulated as an AIE photo-thermal agent and contrast agent into the crosslinked network of PNA nanogels to produce P-TN nanogels (referred to as PN). Subsequently, Dox was incorporated into the nanogels through electrostatic interactions to obtain P-TN-Dox nanogels (referred to as PND). After the PND reaches the tumor site via blood circulation, low pH triggers a burst release of Dox to induce tumour cell death. Under NIR laser irradiation, photothermal generated by light-induced PN can accelerate tumour cell death. Meanwhile, local temperature elevation can also promote drug release, which synergistically produces an effective photochemotherapy effect and complete tumour ablation.

Dox was purchased from Beyotime Technology (Shanghai, China), with a stock solution of 10 mg/mL, and was stored at -20 °C until use. The Cisplatin (CDDP, gold standard treatment), JNK inhibitor SP600125 were purchased from MedChemExpress (MCE, USA).

The primary antibodies used in this study against B-cell CLL/lymphoma 2 (Bcl-2), BCL2 associated X (Bax), E-cadherin (E-ca), N-cadherin (N-ca), Vimentin, and phosphorylated ASK1 (p-ASK1) and the secondary antibody horseradish peroxidase-conjugated affininpure goat anti-rabbit IgG were all purchased from Proteintech (Wuhan, China). The primary antibodies for apoptosis signal-regulating kinase 1 (ASK1), c-Jun N-terminal kinase (JNK), phosphorylated JNK (p-JNK) and glyceraldehyde-3-phosphate dehydrogenase (GAPDH) were all purchased from Servicebio (Wuhan, China). The c-Fos and c-Jun primary antibodies were purchased from ABclonal Technology (Wuhan, China).

#### Laser instrument

The cells treated with different solutions were irradiated with an 808 nm laser at a power density of 0.5 W cm<sup>-2</sup> for 10 min. For the xenograft tumour model, the right dorsal subcutaneous tumour was irradiated with a fixed-power 4 W 808 nm laser for 10 min.

#### Experimental groups

For the in vitro experiments, the groups were divided as follows: PBS as a control group (Group a), PBS with 808 nm laser irradiation (Group b, PBS+L), Dox (Group

c), Dox with 808 nm laser irradiation (Group d, Dox+L), PN (Group e), PN with 808 nm laser irradiation (Group f, PN+L), PND (Group g), and PND with 808 nm laser irradiation (Group h, PND+L).

#### Cell viability assay

The effects of the different groups on cell viability were determined via a Cell Counting Kit-8 (CCK-8; YEASEN Biotechnology, 40203ES60) according to the manufacturer's protocol. The cells were plated in 96-well plates at a density of 5×10<sup>3</sup>/well and treated with fixed wattage NIR for 10 min after different treatments. After incubation for different times, the absorbance at 450 nm was measured via a Victor3 plate reader (Perkin-Elmer, Waltham, MA, USA) following a 1.5 h incubation with CCK-8 reagent (10 µL/well) at 37 °C.

Cell viability is calculated as follows: Cell viability (%) = (OD<sub>treated group</sub> - OD<sub>blank control group</sub>) / (OD<sub>control group</sub> - OD<sub>blank control group</sub>) × 100%. Subsequently, the half maximal inhibitory concentration (IC<sub>50</sub>) was calculated using GraphPad Prism.

According to the research by Gao D et al. [28], the combination index (CI) is calculated as follows: CI = (C<sub>PN+L,50</sub>/IC<sub>PN+L,50</sub>) + (C<sub>Dox+L,50</sub>/IC<sub>Dox+L,50</sub>). In the formula, C<sub>PN+L,50</sub> and C<sub>Dox+L,50</sub> represent the individual concentrations of PN and Dox in the combination treatment of PND+L required to achieve 50% inhibition, respectively. Additionally, IC<sub>PN+L,50</sub> and IC<sub>Dox+L,50</sub> refer to the concentrations of the single drugs when treated alone to reach 50% inhibition. A CI value less than 1 indicates synergistic action, a CI value equal to 1 indicates additive effect, and a CI value greater than 1 indicates antagonistic action.

#### Colony formation assay

The cells from the different groups were plated on 6-well plates at a density of 1×10<sup>3</sup>/well and cultured in a cell incubator at 37 °C and 5% CO<sub>2</sub>. The medium was replaced with fresh medium every 3 days, and after 2 weeks, the cell colonies were fixed with 4% paraformaldehyde (Servicebio, Wuhan, China) for 30 min and then stained with 1% crystal violet (Servicebio, Wuhan, China). Colonies with more than 50 cells were counted.

#### Cell cycle analysis

The different groups were prepared as described above and incubated for 48 h, after which single-cell suspensions were prepared using trypsin without ethylenediaminetetraacetic acid (EDTA) (Servicebio, Wuhan, China). After centrifugation, the cells were fixed with 75% ethanol overnight at 4 °C. The next day, after a single wash, the cells were treated with PBS containing RNase A (final concentration: 100 µg/mL) and propidium iodide (final concentration: 50 µg/mL) for 30 min at room

temperature and then filtered through a 300-mesh nylon filter. The cell cycle distribution was detected via a CytoFLEX S flow cytometer (Beckman, USA), and experimental data were analysed via FlowJo software.

#### **Apoptosis assay by flow cytometry**

The different treatment groups were prepared as described above, and after a 48-hour incubation, single-cell suspensions were prepared using trypsin without EDTA (Servicebio, Wuhan, China). After centrifugation, the cells were double-stained with an Annexin V-FITC/PI apoptosis detection kit (Beyotime, Shandong, China) according to the manufacturer's instructions, incubated in the dark for 30 min, and filtered through a 300-mesh nylon filter. Apoptotic cells were detected via a CytoFLEX S flow cytometer (Beckman, USA), and experimental data were analysed via FlowJo software.

#### **Phalloidin staining**

Different groups of the two cell lines were fixed with 4% paraformaldehyde for 30 min, permeabilised with 0.2% Triton X-100 for 5 min, stained with fluorescent phalloidin solution (Yeasen, Shanghai, China), incubated in the dark for 30 min, and washed three times with PBS. The cell nuclei were stained with 4',6-diamidino-2-phenylindole (DAPI, Servicebio, Wuhan, China) for 2 min. Images were then captured under a fluorescence microscope (Olympus, Japan).

#### **Wound-healing assay**

Cal27 or Tu686 cells were plated in 6-well plates and incubated at 37 °C and 5% CO<sub>2</sub> until the bottom of the well was completely covered with a single layer of cells, and straight lines were generated with the tip of a 200 µl pipette. Images of the scratch healing were taken at 0 h and 48 h. The area of the scratch was measured and analysed via ImageJ software (1.54) to assess the degree of cell migration.

#### **Transwell assay**

Matrigel was diluted at a ratio of 1:8 in serum-free medium, applied to the transwell membrane, and incubated at 37 °C for 1 h. After digestion and centrifugation,  $5 \times 10^4$  cells were resuspended in 200 µL of serum-free medium and added to the transwell chamber. In the lower chamber, medium supplemented with 20% FBS was added, and the culture was continued for 72 h. The transwell chamber was then removed, and nonmigrating cells were discarded. The remaining cells were fixed with 4% paraformaldehyde, stained with 1% crystal violet, and washed. After five different fields of view were examined, the cells were counted via a microscope.

#### **RNA isolation and quantitative reverse transcription polymerase chain reaction (qRT-PCR)**

The cells treated with 0 µg/mL or 5 µg/mL PN were irradiated with a fixed power for 10 min and cultured for 24–48 h, after which total RNA was extracted from the cultured cells using TRIzol. The OD value at 260 nm was measured to calculate the RNA concentration. Total RNA (1 µg) was reverse transcribed via a reverse transcriptase kit (Servicebio, Wuhan, China) according to the manufacturer's protocol. The resulting cDNA (20 ng) was mixed with SYBR-Green Master Mix (Servicebio, Wuhan, China) and amplified via PCR with the appropriate primers.

#### **Western blot (WB)**

Cells treated with PN at 0 µg/mL and 5 µg/mL were irradiated in parallel for 10 min, cultured for 72 h, and lysed in RIPA buffer (Servicebio, Wuhan, China). The protein concentration was determined via a BCA protein assay kit (Beyotime). The lysed proteins (20 µg/lane) were separated by SDS-PAGE (10% gel) and then transferred onto a 0.45 µm PVDF membrane (Millipore, USA). The membrane was blocked with rapid sealing solution (Servicebio, Wuhan, China) at room temperature for 15 min, followed by three washes with 1× TBST for 10 min each. The membrane was incubated with primary antibodies against GAPDH, Bax, Bcl-2, E-ca, N-ca, vimentin, ASK1, p-ASK1, JNK, p-JNK, c-Fos, and c-Jun at a dilution of 1:1000 overnight at 4 °C. On the second day, the membrane was incubated with a goat anti-rabbit IgG secondary antibody at a dilution of 1:3000 for 1 h at room temperature. Finally, the protein bands were visualised via an enhanced chemiluminescence (ECL) imaging system (Chemidoc, Bio-Rad, Hercules, CA, USA). The grey values of the bands were quantitatively measured via Image J (version 1.54).

#### **In vivo xenograft model**

Twenty-five female BALB/c nude mice, aged 4 weeks and weighing 16–18 g, were obtained from the Shulaibao Biotechnology Company in Wuhan, China and housed in the SPF animal room of the Animal Experiment Centre at the People's Hospital of Wuhan University. After one week of adaptive feeding, 100 µL of Cal27 cells suspended in PBS ( $1 \times 10^7$ /mL) were implanted subcutaneously in the right dorsal region of each nude mouse, and the growth of the xenograft was monitored every 2 days. When the tumour volume reached approximately 100 mm<sup>3</sup>, the nude mice were randomly divided into 5 groups (5 mice per group): PBS as a control group (group a), PBS with 808 nm laser irradiation (group b, PBS+L), Dox with 808 nm laser irradiation (group c, Dox+L), PN with 808 nm laser irradiation (group d, PN+L), and PND with 808 nm laser irradiation (group e, PND+L).



On Day 1, groups a-e were injected via the tail vein with 100  $\mu$ L of PBS and 100  $\mu$ L of PBS with Dox (2 mg/kg), PN (4 mg/kg), or PND (4 mg/kg), respectively. Twenty-four hours after administration, groups b-e were anaesthetised with gas, and the tumours were irradiated locally with a fixed power laser at 4 W and 808 nm for 10 min, which was repeated after a 1-day interval. Tumour size and mouse weight were monitored every two days. The tumour volume (TV) was calculated via the formula  $TV (\text{mm}^3) = 0.5 \times a^2 \times b$ , where  $a$  is the shortest diameter and  $b$  is the longest diameter. The relative tumour volume (RTV) was calculated via the formula  $RTV = V_t / V_0$ , where  $V_0$  is the initial tumour volume and  $V_t$  is the tumour volume on day  $t$ . The tumour inhibition rate (TIR) was calculated via the formula  $TIR(\%) = (1 - RTV_{\text{treated}} / RTV_{\text{control}}) \times 100\%$ , where  $RTV_{\text{treated}}$  is the relative tumour volume of the mice treated with various drugs, and  $RTV_{\text{control}}$  is the relative tumour volume of the mice in the blank control group. After 14 days, all the nude mice were euthanised, and the tumours and major organs (heart, liver, spleen, lung, and kidney) were immediately excised from the mice.

#### Histopathological examination (HE)

Tumour and major organ sections were stained with haematoxylin and eosin via a standard protocol. After dehydration and clearing with ethanol and xylene, images were captured via a microscope (Olympus, Japan).

#### Immunofluorescence (IF)

The protein levels in the tumour tissues were detected via immunofluorescence. The tumour tissue sections were deparaffinised and hydrated with a gradient of ethanol. After antigen retrieval, the sections were treated with a 10% bovine serum albumin (BSA; Yamei, Shanghai, China) solution for 60 min. The sections were subsequently incubated with primary antibody (1:800) overnight. Then, the sections were incubated with a fluorescent secondary antibody (1:500) in the dark. The cell nuclei were then stained with DAPI (5  $\mu$ g/mL).

#### Statistical analysis

Data with a normal distribution are presented as the mean  $\pm$  standard deviation (mean  $\pm$  SD). Comparisons between groups for normally distributed quantitative data were made via  $t$  tests or one-way ANOVA. All the data were analysed and plotted via GraphPad Prism 10.1.2 software (GraphPad, USA). A  $p$  value of less than 0.05 was considered statistically significant. For each experiment, when the  $p$  value was greater than 0.05, it was indicated as ns; when the  $p$  value was less than 0.05, it was indicated as \*; when it was less than 0.01, it was indicated as \*\*; when it was less than 0.001, it was indicated as \*\*\*; and when it was less than 0.0001, it was

indicated as \*\*\*\*. For the in vitro experiments, compared with PBS+L group,  $\#p < 0.001$ . Compared with PN+L group,  $+p < 0.001$ ,  $\sim p > 0.05$ .

## Results

### PN and PND inhibited the proliferation of HNSCC cells

The chemical structures of PN and PND are shown in Fig. 1A. We evaluated the effects of PN and PND on cell proliferation through CCK-8 and colony formation assays.

Firstly, to explore whether the combination treatment of the two drugs plus phototherapy has a synergistic or antagonistic effect, according to the combination index formula, we calculated the IC<sub>50</sub> values of PND+L, PN+L, and Dox+L on two HNSCC cell lines after 48 h of treatment, as shown in Fig. 1B-C. The calculated combination indices of Cal27 and Tu686 cells were 0.571 and 0.837, respectively, which were less than 1, confirming the synergistic effect of PN+L and Dox+L added to PND+L.

Furthermore, the experimental results showed that the IC<sub>50</sub> values of PN+L treatment group in Cal27 cells and Tu686 cells were 5.04 and 4.032, respectively, so the subsequent PN working concentration was selected as 5  $\mu$ g/mL. Based on previous experiments, the fixed ratio of PN and Dox in PND was set to 2:1. With the PN concentration fixed to 5  $\mu$ g/mL, the Dox concentration in PND was selected to 2.5  $\mu$ g/mL, so the Dox concentration used alone was also 2.5  $\mu$ g/mL. The IC<sub>50</sub> values of the CDDP group in Cal27 cells and Tu686 cells was 4.923 and 4.76, respectively, so the subsequent working concentration of the CDDP group was determined to be 5  $\mu$ M.

In addition, to assess the effects of Dox+L, PN+L, PND+L, and CDDP on healthy cells, HOK cell line (normal oral epithelial keratinocytes) was used for supplementary CCK8 assay. The time gradients (24, 48 h) and concentration gradients were set to calculate the cell survival rate, as shown in Fig. 1D-G. Our experimental results revealed that the PN+L had the least effect on the vitality of HOK cells, whereas the Dox+L and CDDP group were more toxic to normal cells. Notably, at the same concentration of Dox, the PND+L group demonstrated a markedly lower toxicity to HOK cells than that of Dox+L group, which could play a role in reducing the toxic side effects of Dox.

In the two HNSCC cell lines, CCK8 assays were conducted on eight treatment groups to record the OD values and perform statistical analysis among the groups (Fig. 1H-I). Compared with the control cells, the cells treated with NIR irradiation alone did not significantly inhibit proliferation in either HNSCC cell line. There was no significant difference in cell proliferation between the Dox group and the Dox+L group. However, compared

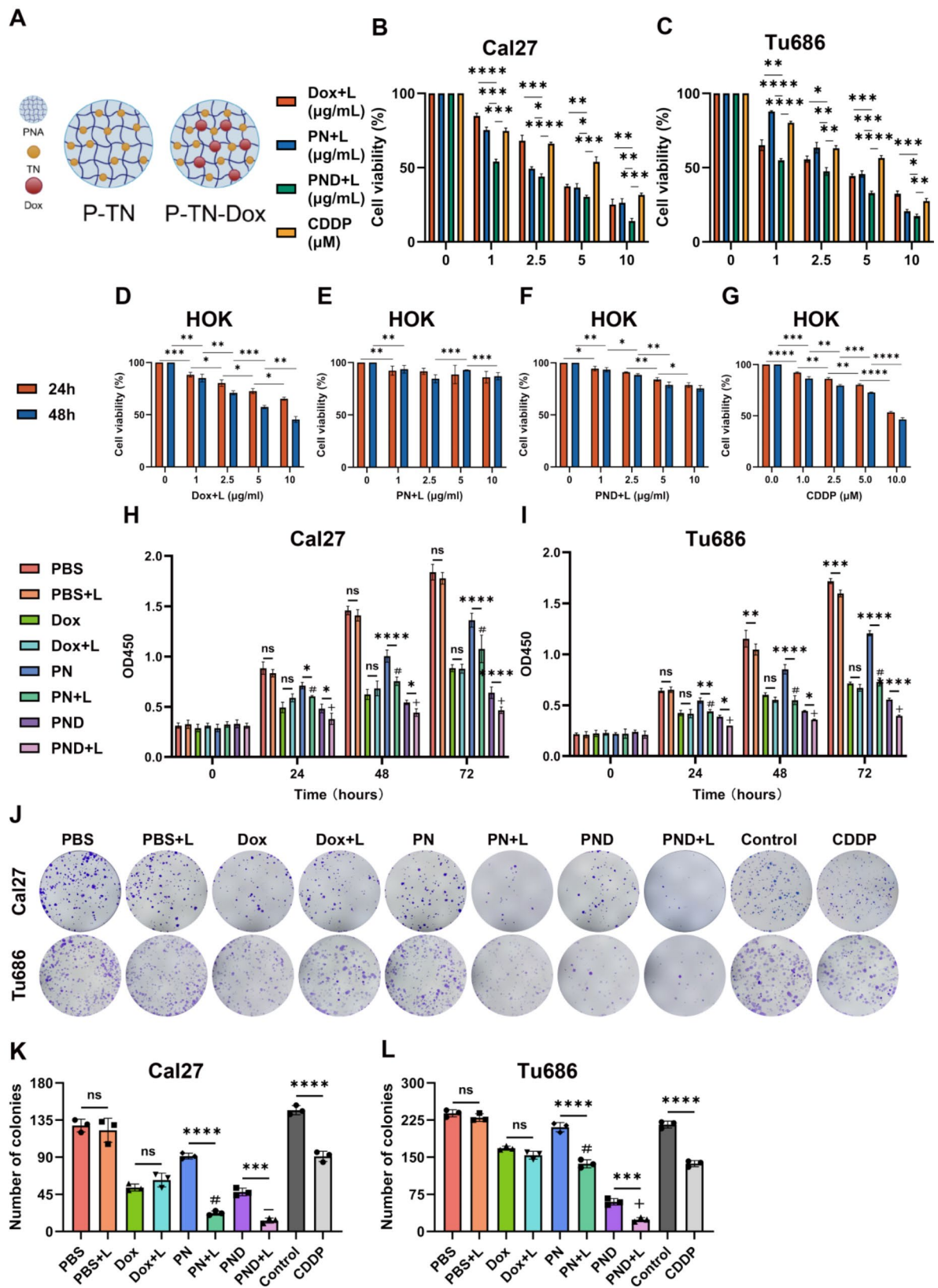


Fig. 1 (See legend on next page.)

(See figure on previous page.)

**Fig. 1** PN and PND inhibited the proliferation of HNSCC cell. **A** 2D structures of PN and PND. **B-C** Cal27 and Tu686 cells were treated with various concentrations of Dox + L, PN + L, PND + L, CDDP for 48 h, and then cell viability was assessed using the CCK-8 assay. **D-G** HOK cells were treated with various concentrations of Dox + L, PN + L, PND + L, CDDP for 24 h and 48 h, and then cell viability were assessed using the CCK-8 assay. **H-I** Cal27 and Tu686 cells were divided into eight groups and treated for 24 h, 48 h, and 72 h, and then OD values was assessed using the CCK-8 assay. **J-L** The colony formation assay was used to detect the colony formation of Cal27 and Tu686 cells in different treatment groups. Colony numbers were quantified. \* $p < 0.05$ , \*\* $p < 0.01$ , \*\*\* $p < 0.001$ , \*\*\*\* $p < 0.0001$ . Compared to PBS + L group: # $p < 0.001$ . Compared to PN + L group: + $p < 0.001$ ,  $\bar{p} > 0.05$ . All data are shown as the mean  $\pm$  SD from three independent experiments

with the PN group, the PN+L group presented a more significant inhibitory effect on HNSCC cell proliferation.

The colony formation assay revealed that, compared with drug treatment or single NIR irradiation, PND+L significantly hindered the colony formation ability of HNSCC cells (Fig. 1J-L). In Cal27 cells, there was no difference in colony formation ability between PND+L and PN+L, possibly due to the strong inhibitory effect of PN+L, and the inhibited colony formation ability after combination drug treatment did not significantly differ; however, in Tu686 cells, there was a significant difference in the inhibition rate between the PND+L group and the PN+L group. In summary, the experimental results indicated that photothermal chemotherapy, i.e., the PND+L treatment group used in this study, had a strong synergistic effect on the inhibition of tumour cell aggregation.

#### PN and PND induced the apoptosis of HNSCC cells

Cell proliferation is reported to be closely intrinsically linked to cell cycle progression [29]. To gain a deeper understanding of the effects of two new types of nano-drugs on the proliferation of HNSCC, we measured the fluorescence intensity of the PI-DNA complex within cells via FlowJo software to calculate the cell cycle distribution (Fig. 2A-C). After the addition of NIR irradiation, there was no significant difference in the cell cycle distribution between the PN+L group and the PN-only group. Compared with the blank control group, the Dox and PND groups presented clear arrest at the G2/M phase, and the proportion of cells arrested at the G2/M phase remained greater than that of the PBS+L group even after the addition of NIR irradiation.

Next, we used flow cytometry to assess the impact of different treatment combined with NIR irradiation on the apoptosis of HNSCC cells (Fig. 2D-F). The cells were double-stained with FITC-annexin V/PI, and data analysis was performed via FlowJo software. The total apoptosis rate was calculated as the sum of the percentages of FITC-positive cells (FITC+). Our study revealed that, in Cal27 and Tu686 cells, there was no significant difference in the rate of apoptosis between the PBS group and Dox group and their respective laser-irradiated groups (PBS+L and Dox+L). However, compared with the PN group, the PN+L group presented a significant increase in cell apoptosis. Furthermore, compared with the PND group, the PND+L group exhibited a significantly greater rate of cell apoptosis. In both types of HNSCC cells, the

apoptosis rate in the PND+L group was significantly greater than that in the PN+L group, which is consistent with the results of the CCK-8 and colony formation assays.

This study subsequently used qRT-PCR and WB detection to assess the mRNA and protein levels of apoptosis-related genes (Fig. 2G-I, Fig S1 A-B). Compared with that in the PBS+L group, the expression of the proapoptotic Bax mRNA and protein was significantly increased, whereas the expression of the antiapoptotic Bcl-2 mRNA and protein was significantly reduced in the PN+L group.

#### PN and PND inhibited the migration, invasion and EMT ability of HNSCC cells

To assess the impact of PN and PND on cell migration, invasion and epithelial-mesenchymal transition (EMT) ability, phalloidin staining was conducted for cytoskeleton, wound healing, and transwell assays. The selected concentrations of PN and PND (1  $\mu$ g/mL) induced less than 20% inhibition of HNSCC cell proliferation, minimising the potential confounding effects of proliferation inhibition on migration and invasion.

Phalloidin staining was used to detect skeletal changes in HNSCC cells after treatment with Dox, PN, PND, or NIR (Fig. 3A). Compared with untreated control cells, cells treated with NIR alone presented minimal morphological changes. The cytoskeletal structures of Cal27 and Tu686 cells, including cell lamellipodia and stress fibres, were reduced to varying degrees after treatment with various drugs with or without NIR. In both cell lines, the PND+L group presented the most epithelial-like cell morphology, with fewer surrounding pseudopodia, suggesting that the PND+L group had the weakest ability to migrate and infiltrate the surroundings.

To further evaluate the occurrence of EMT, we conducted a scratch test to assess cell migration (Fig. 3B-C). In the Cal27 and Tu686 cell lines, there was no significant difference in the cell migration rate between the PBS+L group and the PBS group. Similarly, there was no significant difference in the migration rate between the Dox group and the Dox+L group. In contrast, in the PN+L group, the HNSCC cell migration rate was significantly lower than that in the PN group. In the Tu686 cell line, the PND+L group clearly inhibited migration compared with the PND-only group, whereas in the Cal27 cell line, there was no significant difference in the migration rate between the PND and PND+L groups, possibly

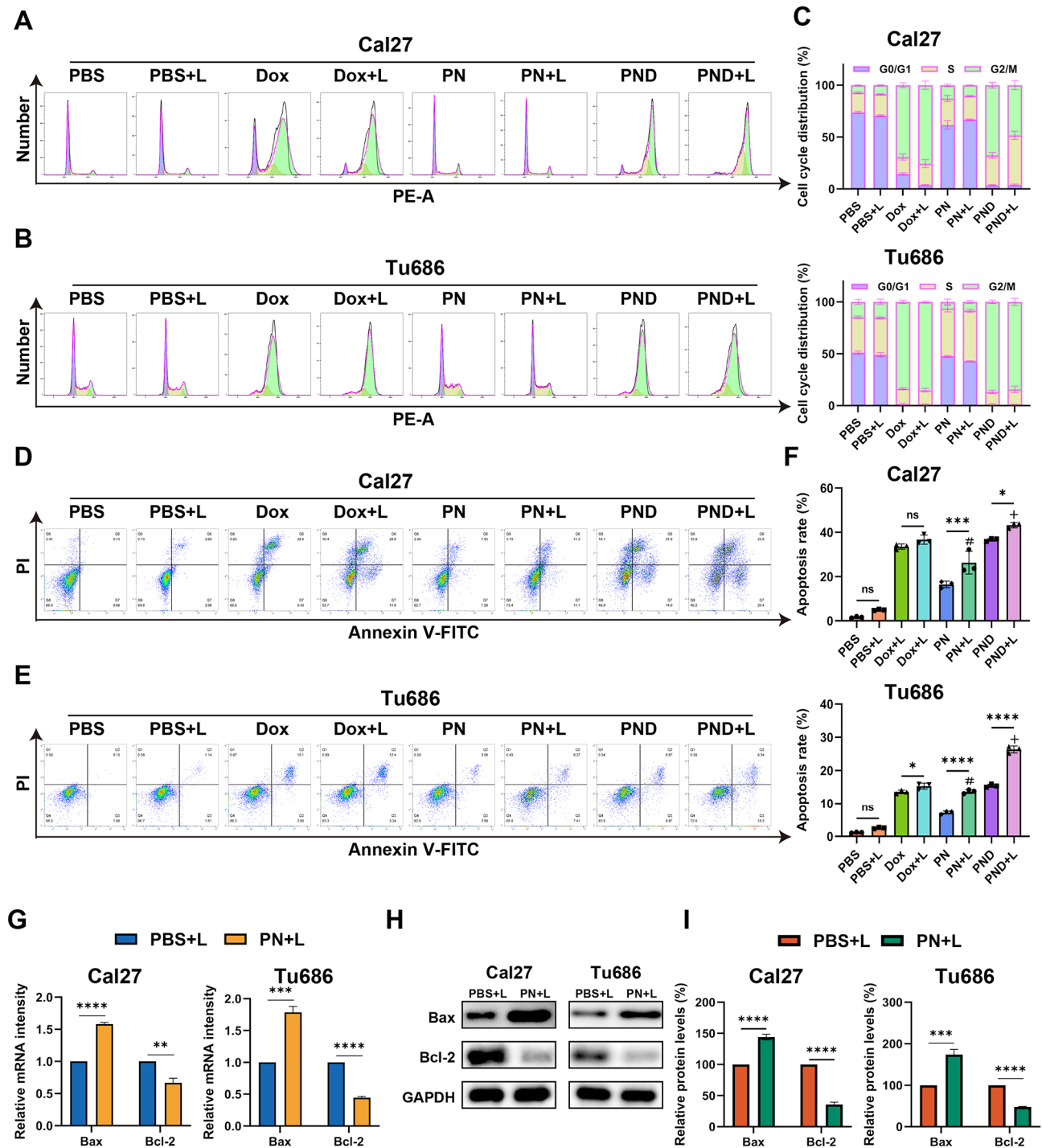


**Fig. 2** PN and PND induced cell apoptosis of HNSCC cells. **A-C** Cal27 and Tu686 cells were treated with different interventions, and the cell cycle was assessed by flow cytometry. **D-F** Cal27 and Tu686 cells were treated with different interventions, and the apoptosis rate was assessed by flow cytometry. **G** Cal27 and Tu686 cells were treated with PBS + L or PN + L for 48 h. The mRNA levels of Bax, Bcl-2 were assessed using qRT-PCR. **H-I** Cal27 and Tu686 cells were treated with PBS + L or PN + L. The protein levels of Bax, Bcl-2 were assessed using Western blotting. \* $p < 0.05$ , \*\* $p < 0.01$ , \*\*\* $p < 0.001$ , \*\*\*\* $p < 0.0001$ . Compared to PBS + L group: # $p < 0.001$ . Compared to PN + L group: + $p < 0.001$ , ~ $p > 0.05$ . All data are shown as the mean  $\pm$  SD from three independent experiments



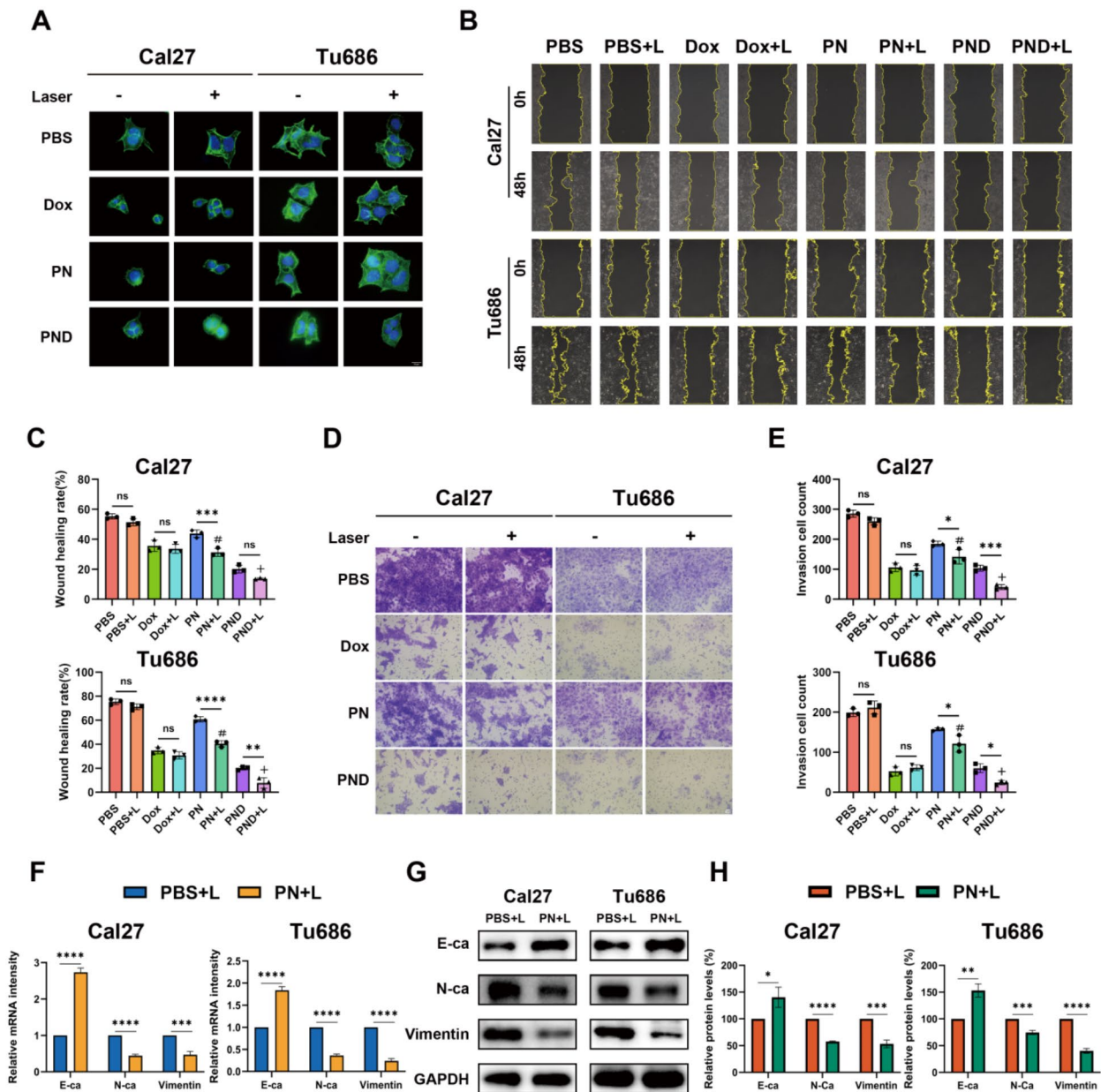


**Fig. 3** PN and PND inhibited cell migration, invasion and EMT ability of HNSCC cells. **A** Cal27 and Tu686 cells were treated with different interventions, and the Phalloidin staining was observed by microscope. Scale bar: 10  $\mu$ m. **B-C** Wound healing assay assessed the migration ability of Cal27 and Tu686 cells treated with different interventions. Statistical results of wound closure were presented. Scale bar: 50  $\mu$ m. **D-E** Transwell invasion assay determined the number of HNSCC cells penetrating the lower chamber and captured images using microscopy. Statistical results were presented. Scale bar: 50  $\mu$ m. **F** Cal27 and Tu686 cells were treated with PBS + L or PN + L for 48 h. The mRNA levels of E-cadherin, N-cadherin and Vimentin were assessed using qRT-PCR. **G-H** Cal27 and Tu686 cells were treated with PBS + L or PN + L. Protein levels of E-cadherin, N-cadherin and Vimentin were assessed using Western blotting. Compared to PBS + L group: # $p < 0.001$ . Compared to PN + L group: + $p < 0.001$ ,  $\bar{p} > 0.05$ . All data are shown as the mean  $\pm$  SD from three independent experiments

because of the strong baseline inhibitory effect of PND on cell migration, making the effect of adding NIR statistically insignificant. Furthermore, compared with the PBS+L group, the PN+L group presented obviously limited migration, and the PND+L group presented the most significant migration inhibition in both HNSCC cell lines. The invasive ability of the cells was further assessed

via the Matrigel invasion assay, and the results were consistent with those of the wound healing test (Fig. 3D-E).

To understand the underlying mechanism of the inhibitory effect of PN on HNSCC cell migration and invasion, we studied its impact on EMT (Fig. 3F-H, Fig S1 C-D). In both Cal27 and Tu686 cells, after treatment with PN+L, the expression of the epithelial marker E-ca at the



mRNA and protein levels increased, whereas the expression of the mesenchymal markers N-ca and vimentin significantly decreased compared with that in the PBS+L group.

**PN induced apoptosis and inhibited proliferation and EMT ability via the JNK pathway**

A previous study clearly established the pivotal role of the JNK signalling pathway in drug-induced cell proliferation, apoptosis, and EMT [30]. To elucidate the precise

mechanism by which PN+L affects HNSCC cells, we examined the expression levels of key proteins in the JNK signalling cascade. In Cal27 and Tu686 cells, treatment with PN+L significantly increased the levels of p-ASK1, p-JNK, c-Jun, and c-Fos without altering the total protein levels of ASK1 and JNK (Fig. 4A-B).

In subsequent experiments, to confirm these findings and explore the specificity of the mechanism, we treated HNSCC cells with the specific JNK inhibitor SP600125 for rescue experiments. Protein immunoblotting analysis

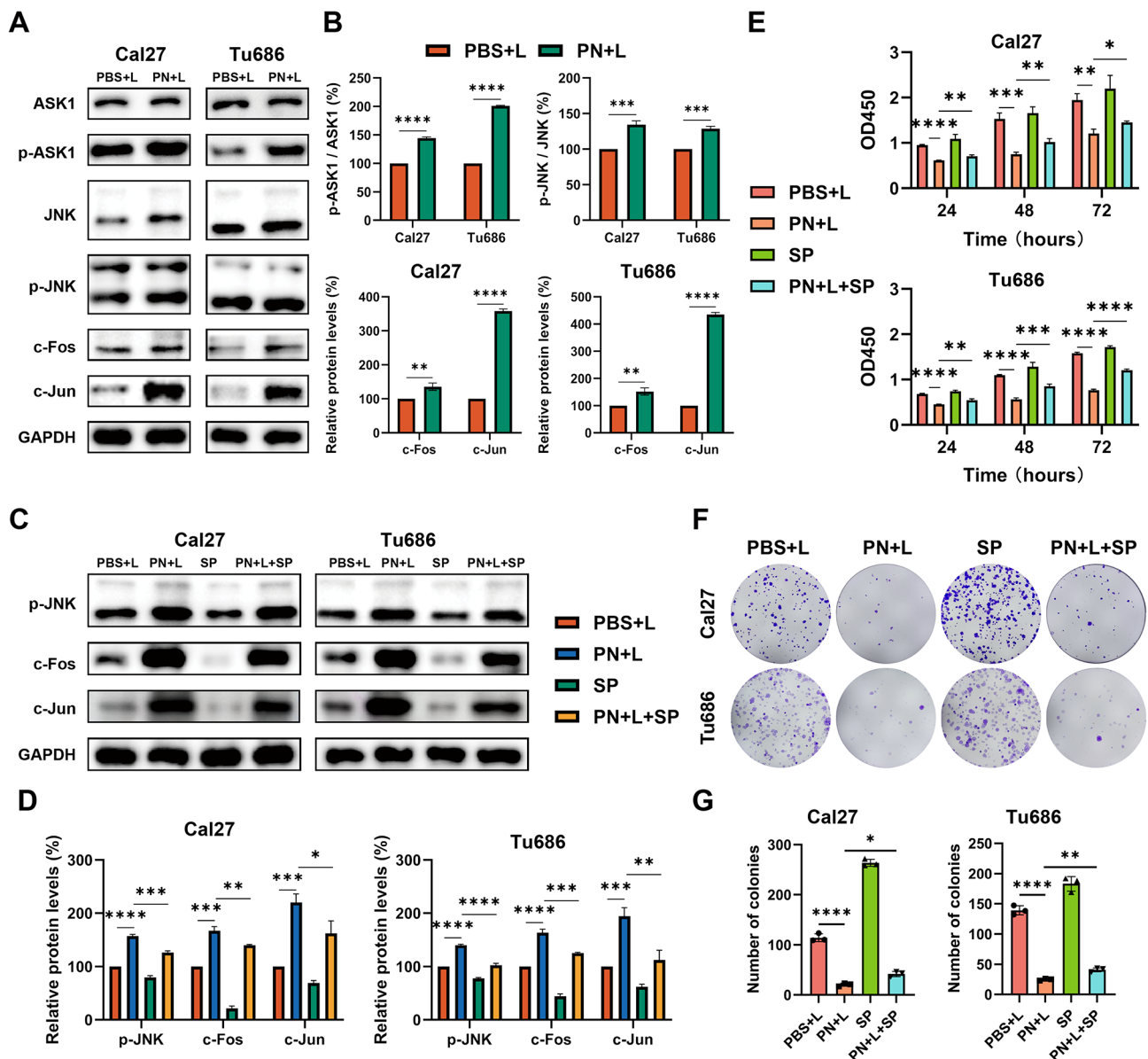


**Fig. 4** PN inhibited the proliferation of HNSCC via the JNK pathway. **A-B** Western blotting detected the key protein levels of the JNK pathway in PN+L-treated Cal27 and Tu686 cells, along with the statistical analysis. **C-D** Protein changes of p-JNK, c-Fos and c-Jun in Cal27 and Tu686 cells treated or untreated with PN+L and SP600125 were detected by Western blotting. Statistical analysis is presented. **E** CCK-8 assay was used to detect the cell viability of Cal27 and Tu686 cells treated with PN+L for 48 h with or without SP600125. **F-G** Colony formation assay of PN+L-treated HNSCC cells with or without SP600125 treatment. Quantitative analysis of colony numbers. \* $p < 0.05$ , \*\* $p < 0.01$ , \*\*\* $p < 0.001$ , \*\*\*\* $p < 0.0001$ . All data are shown as the mean  $\pm$  SD from three independent experiments

revealed that SP600125 (0.5 μM) significantly decreased the levels of p-JNK and the downstream pathway proteins c-Fos and c-Jun in HNSCC cells treated with PBS+L or PN+L (Fig. 4C-D). We subsequently investigated the impact of inhibiting JNK on the phenotypic changes induced by PN+L in HNSCC cells. Using CCK-8 and colony formation assays, we observed that SP600125 partially mitigated the inhibitory effects of PN+L on the proliferation and colony formation of HNSCC cells

(Fig. 4E-G). Flow cytometry analysis revealed that, compared with treatment with PN+L alone, cotreatment with SP600125 significantly reduced the apoptosis rate of HNSCC cells (Fig. 5A-B). Furthermore, SP600125 partially counteracted the inhibitory effect of PN+L on the migratory ability of HNSCC cells (Fig. 5C-D). Protein immunoblotting analysis revealed that SP600125 partially reversed the changes in the protein levels of Bax, Bcl-2, E-ca, N-ca, and vimentin induced by PN+L. (Fig. 5E-G).

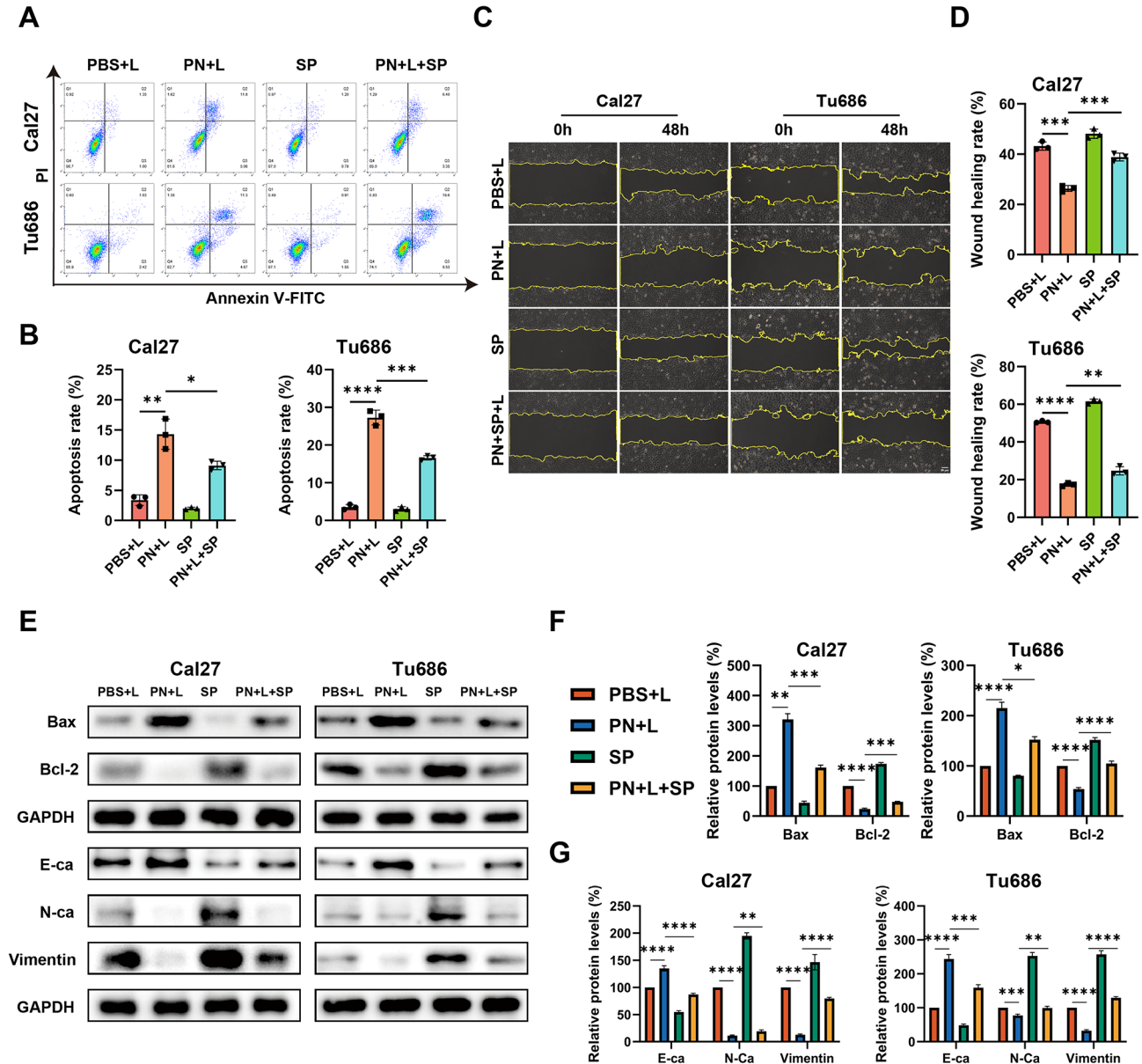


**Fig. 5** PN induced apoptosis and inhibited EMT ability via the JNK pathway. **A-B** Cal27 and Tu686 cells treated or untreated with PN+L and SP600125, and the apoptosis rate was assessed by flow cytometry. **C-D** Wound-healing assay was used to detect the migration of PN+L-treated HNSCC cells with or without SP600125. Scale bar: 50 μm. **E-G** Cal27 and Tu686 cells treated or untreated with PN+L and SP600125, and the protein levels of Bax, Bcl-2, E-cadherin, N-cadherin and Vimentin were assessed using Western blotting. Statistical analysis is presented. \**p* < 0.05, \*\**p* < 0.01, \*\*\**p* < 0.001, \*\*\*\**p* < 0.0001. All data are shown as the mean ± SD from three independent experiments

### PN and PND exerted antitumour effect on HNSCC in vivo

On the basis of the findings from our cellular experiments, we used a nude mouse xenograft tumour model to further investigate the in vivo biological effects of PN and PND. Figure 6A displays the animal experimental procedure. Over time, there were no significant differences in the body weights of the tumour-bearing mice in all the groups or in the histological morphology of important organs in the four drug-treated groups, indicating that the therapeutic intervention was well tolerated (Fig. 6B and G). After completing the 14-day treatment regimen, the tumour growth in the blank control group and the NIR treatment group was rapid, whereas the tumour progression in the other three groups significantly slowed, with the PND+L group showing the most pronounced reduction (Fig. 6C). Compared with the tumour volume at the end of the study in the blank control group, the TIRs for the Dox+L, PN+L, and PND+L groups were 65.37%, 79.28%, and 90.62%, respectively (Fig. 6D).

Posttreatment necropsy and subsequent tumour weight measurements revealed that the average tumour weights for the PBS, PBS+L, Dox+L, PN+L, and PND+L groups were 0.372 g, 0.306 g, 0.172 g, 0.112 g, and 0.054 g, respectively (Fig. 6E-F). Among them, the PND+L group had the least massive tumours, coupled with the most massive TIR, indicating that this group had the best therapeutic effect, once again confirming the superior synergistic effect of PND-mediated chemo-photothermal therapy.

Furthermore, the expression levels of proteins related to apoptosis, EMT, and the JNK signalling pathway in animal tumour tissues were detected via IF. The results revealed that the expression of Bax, E-ca, p-Ask1, p-JNK, c-Fos, and c-Jun increased to varying degrees, whereas the expression of Bcl-2, N-ca, and vimentin decreased. These changes were consistent with the mRNA and protein expression data from the in vitro experiments. These findings confirmed that PN+L intervention, through the JNK signalling pathway, delayed the progression of HNSCC both in vivo and in vitro (Fig. 6H-I).

### Discussion

Currently, the conventional treatment for locally advanced HNSCC patients often employs a combination of surgery, radiotherapy, and chemotherapy, but typically, only approximately 50% of patients experience significant therapeutic effects [31]. In recent years, advancements in anticancer drug therapies have been rapid, with their importance increasing annually [32]. However, since effective treatment outcomes usually require high doses of drugs, monotherapy inevitably leads to noticeable systemic side effects. Therefore, developing drugs with dual antitumour effects and synergistic nanotherapy systems

to achieve high therapeutic efficiency and minimal side effects may be a potential solution to this problem [33].

The combination of chemotherapy and photothermal therapy, which is characterised by noninvasiveness, precise spatiotemporal control, and low toxicity, offers significant advantages and has encouraged the research and development of multimodal nanomedical approaches [10]. Research by Wan et al. [34] has shown that charge-reversal polymeric nanoparticles (MPPD@IR825/DTX NPs) serve as an effective platform for synergistic chemophotothermal therapy, with markedly improved efficacy and fewer toxic side effects than monotherapies of chemotherapy or photothermal therapy. However, traditional organic fluorophores have fatal limitations in terms of aggregation-caused quenching (ACQ) effects [35]. In contrast, AIE fluorophores exhibit outstanding advantages, such as high emission intensity in aggregated states, large Stokes shifts, remarkable photostability, and high in vivo on-off capability, providing a viable alternative for constructing synergistic therapies [36].

PN and PND, the novel materials used in this study, have been validated for their therapeutic efficacy in 4T1 breast cancer cells and a mouse model of orthotopic breast cancer [27]. However, the potential of PN and PND as novel anticancer drugs for HNSCC treatment has not been reported. On the basis of these findings, the present study investigated their effects on HNSCC proliferation, apoptosis, and metastatic phenotypes through in vitro and in vivo models. The results of this study confirmed that the efficacy of PN with or without light exposure significantly differed in terms of cell proliferation, apoptosis, invasion, migration, and EMT phenotypes, indicating that PN, as a new type of nanomaterial, must exert its anticancer effects through photothermal therapy after NIR treatment. Moreover, PND, which is a functionalised nanogel based on AIE, effectively integrates the chemotherapeutic drug Dox, thereby synergistically producing effective chemothermal therapy and complete tumour ablation, with significantly superior anticancer efficacy compared with PN combined with NIR treatment alone. Furthermore, at the same Dox concentration, PND+L group has less toxicity to normal oral epithelial cells. The reason may be that PND is required to trigger a burst release of Dox at low pH to induce cell death. The pH value in the environment of normal oral epithelial cells is higher than that in the tumour microenvironment, resulting in a low Dox release efficiency.

The Bax/Bcl-2 apoptotic signalling pathway, as a regulator of cell apoptosis and survival, is associated with the occurrence and development of many diseases, where the Bcl-2 family plays a key role in promoting or inhibiting the intrinsic apoptotic pathway triggered by mitochondrial dysfunction [37, 38]. Bax is a key executor of the mitochondrial regulation of cell death, and



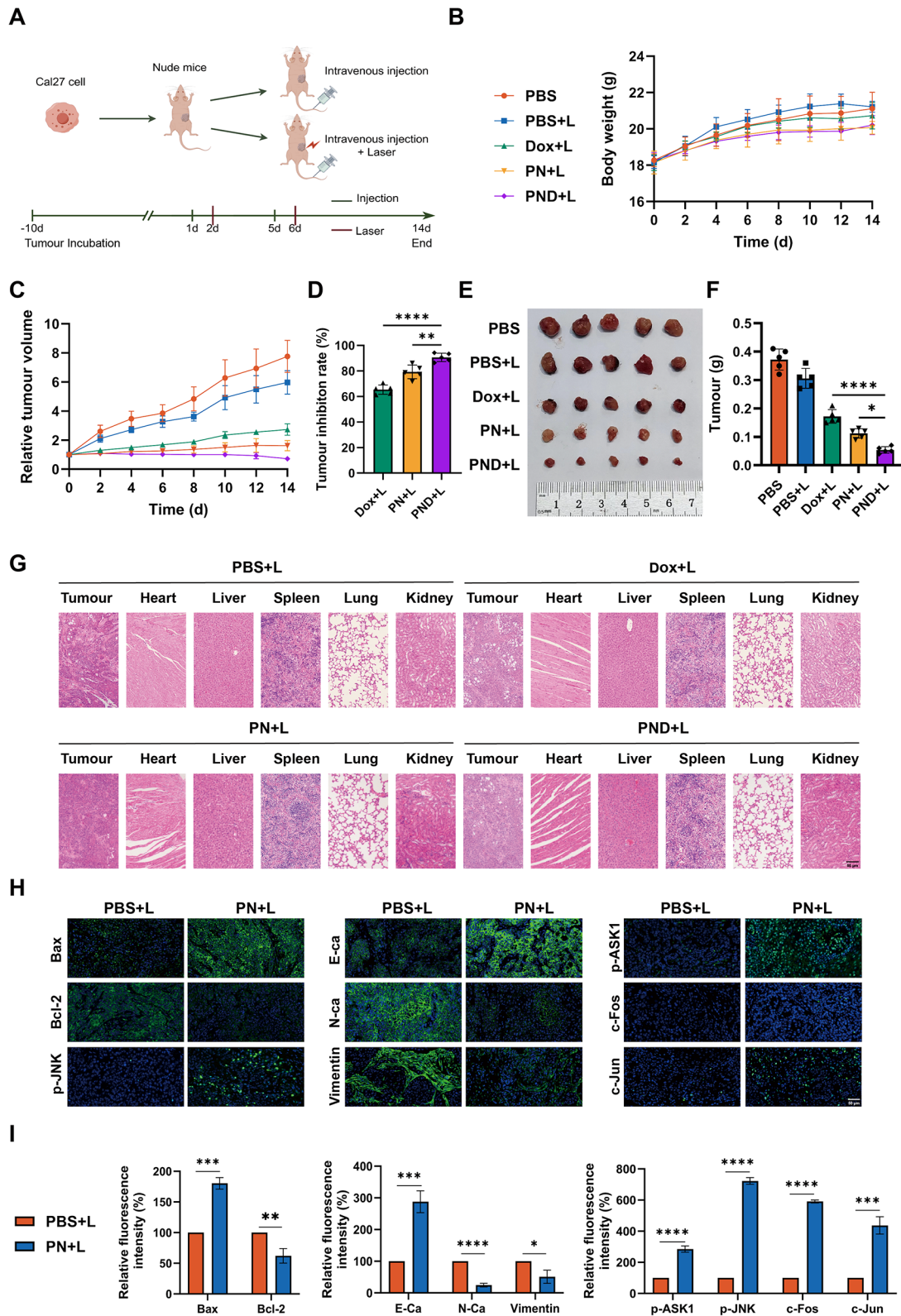


**Fig. 6** PN and PND exerted antitumour effect on HNSCC in vivo. **A** The procedure for the xenograft tumour model in nude mice. **B** The body weight of nude mice was measured every 2 days. **C** Tumour volume was measured every 2 days. **D** The tumour inhibition rate was calculated after death of nude mice. **E** Morphological images of xenograft tumours. **F** Tumour weight at the end of the experiment. **G** HE staining of transplanted tumours, heart, liver, lung, and kidney in nude mice. Scale bar: 50  $\mu$ m. **H-I** IF staining of Bax, Bcl-2, E-cadherin, N-cadherin and Vimentin, p-ASK1, p-JNK, c-Fos and c-Jun, along with quantitative analysis of staining intensity. Scale bar: 50  $\mu$ m. \* $p$  < 0.05, \*\* $p$  < 0.01, \*\*\* $p$  < 0.001, \*\*\*\* $p$  < 0.0001. All data are shown as the mean  $\pm$  SD from three independent experiments

its increased expression can increase the sensitivity of tumour cells to apoptosis [39]. During the course of this study, we observed an increase in the rate of cell apoptosis after treatment with PN+L and PND+L, with the proapoptotic effect of PND+L being more pronounced. The results from WB and PCR indicated that after PN+L treatment, the expression levels of Bax and the Bax/Bcl-2 ratio significantly increased, whereas the expression of Bcl-2 significantly decreased, compared with that of NIR alone in both HNSCC cell types. These molecular changes were further validated in a xenograft tumour model: the changes in the expression levels of Bax and Bcl-2 after PN+L treatment were consistent with the results of the *in vitro* experiments. These results confirm that PN, after NIR treatment, regulates Bax/Bcl-2 apoptotic signalling to promote apoptosis in HNSCC.

HNSCC is an aggressive cancer with strong invasive and metastatic capabilities. One of the key pathways for tumour cell migration and invasion is EMT, which is characterised by the transition of epithelial cells to a mesenchymal phenotype, enhancing cell migration and invasion capabilities [40]. Changes in cell adhesion junctions are considered one of the hallmarks of cancer invasion and progression [41]. In epithelial malignancies, especially squamous cell carcinomas, the main component of these adhesion molecules is E-cadherin [42]. Phalloidin, which tightly binds to filamentous actin, can be used to reveal the cytoskeletal structure [43]. This study revealed through phalloidin experiments that after various drug treatments, the Cal27 and Tu686 cell morphologies tended to favour epithelial cells, with inhibited EMT capabilities. Scratch and invasion assays revealed that after NIR treatment with PN and PND, cell migration and invasion were significantly inhibited, with the PND+L group showing a significantly greater inhibition rate than PN+L or the traditional chemotherapeutic drug Dox. The PCR and WB results revealed a significant increase in the expression of the epithelial marker E-cadherin, whereas the expression of mesenchymal markers, including N-cadherin and vimentin, decreased. The IF staining of the xenograft tumours indicated that the changes in the expression of the aforementioned EMT-related proteins in the PN+L group were consistent with the findings of the *in vitro* experiments, with a marked increase in epithelial cell marker expression and a significant decrease in mesenchymal phenotype marker expression. This series of experiments demonstrated that PN+L inhibits

the migration and invasion of HNSCC cells, with the underlying mechanism being the suppression of EMT.

The JNK signalling pathway has dual roles in different types of cancer [44]. The JNK pathway is disrupted by various factors, such as cytokines, growth factors, reactive oxygen species (ROS), pathogens, and drugs, thereby affecting a series of cellular activities. In HNSCC, the JNK pathway has been shown to act alone or in synergy with other MAPK pathways to exert either oncogenic or tumour-suppressive effects [45–48]. In this study, PCR and WB results revealed that PN+L activates the JNK pathway by promoting the phosphorylation of ASK1, which subsequently activates its downstream target proteins c-Fos and c-Jun. These transcription factors are involved in regulating different cellular responses, such as the proliferation, apoptosis, and EMT processes investigated in this study, thereby delaying the malignant progression of HNSCC. To confirm this finding and explore the specificity of the JNK pathway, we conducted rescue experiments using the JNK inhibitor SP600125. The results showed that SP600125 partially negated the inhibitory effects of PN+L on HNSCC cell proliferation, migration, and invasion; partially inhibited the proapoptotic effects induced by PN+L; and mitigated the impact of PN+L on tumour cell EMT. These results collectively confirm that PN+L specifically and effectively treats HNSCC through the JNK signalling pathway (Fig. 7).

However, this study also has several limitations. Firstly, this study used only two HNSCC cell lines to verify the effects of PN and PND *in vitro*. In the future, more HNSCC cell lines could be used to fully validate the anti-cancer efficacy of the new nanomaterials PN and PND. Secondly, we will conduct animal experiments to investigate the difference in efficacy and toxicity between the novel photochemotherapy dual-functional drug delivery nanosystem and the HNSCC gold standard treatment (CDDP). Additionally, in order to adapt to the needs of preclinical research of drugs in the future, more xenograft and metastatic tumour models will be studied to determine the efficacy and targeting characteristics of this drug against head and neck tumours. Lastly, from a mechanistic perspective, we focused only on the impact of PN+L on the JNK signalling pathway, but the specific mechanism of the more efficacious photochemotherapy dual system PND+L was not elucidated in this study. These issues warrant further research in the future.



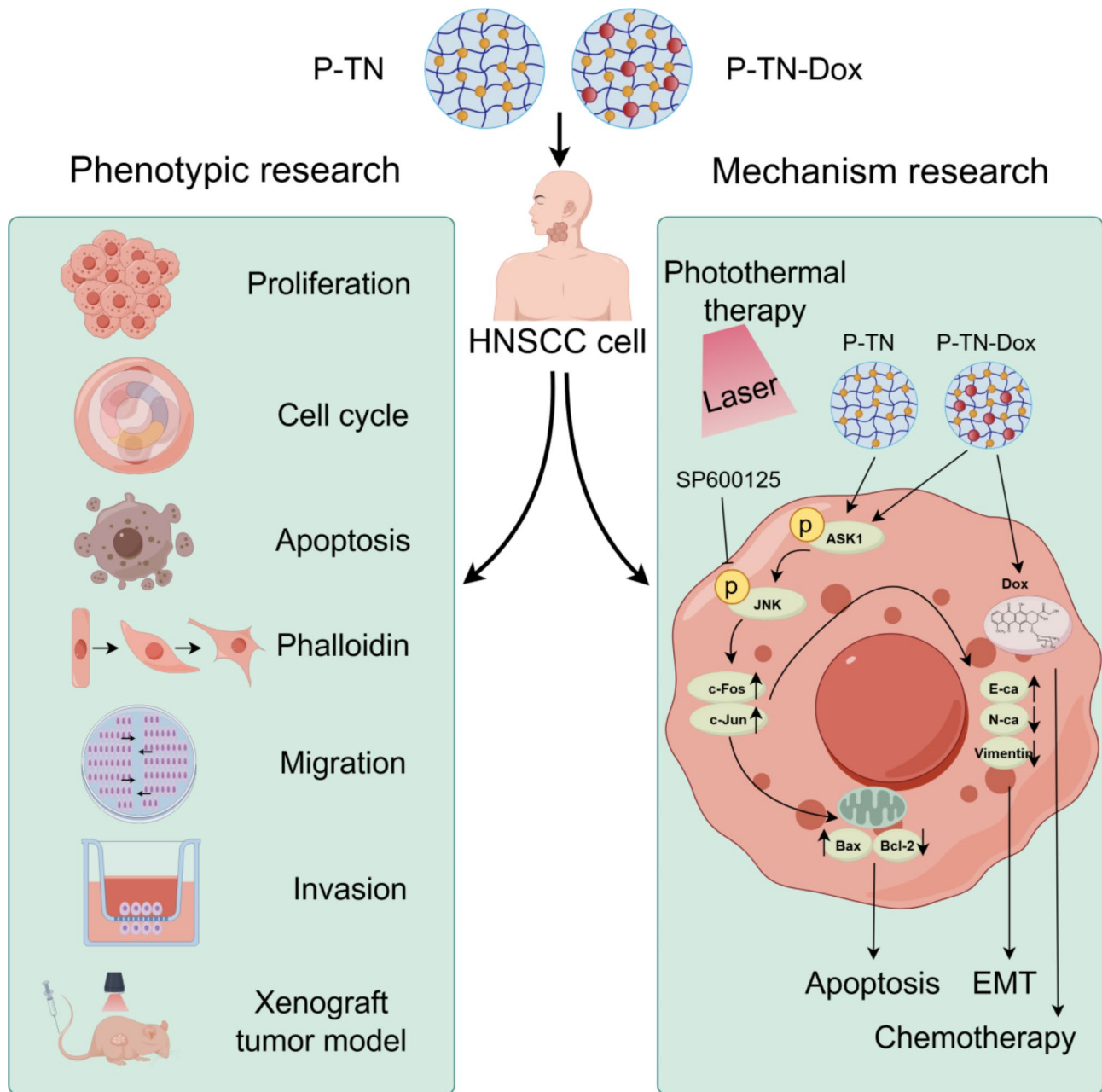


**Fig. 7** Schematic diagram of nanomedicine anti-tumour activity on HNSCC cells by activating the JNK signalling pathway. This illustration was generated by Figdraw

**Conclusion**

In summary, our study revealed that the PN+L and PND+L treatments significantly inhibited the proliferation, metastatic and EMT capabilities of HNSCC while inducing cell apoptosis. The therapeutic effect of PND+L was markedly stronger than that of PN+L. Our research also revealed that PN+L promotes the apoptosis of HNSCC cells by activating the JNK signalling pathway. The combination of photochemotherapy, namely, PND+L, shows greater efficacy in inhibiting tumour

growth and holds promise as a new potential therapeutic approach for HNSCC.

**Supplementary Information**

The online version contains supplementary material available at <https://doi.org/10.1186/s12967-024-05855-8>.

Supplementary Material 1

**Supplementary Material 2: Figure S1.** PN and PND affect the apoptosis and EMT ability of HNSCC cell line. **A-B** Cal27 and Tu686 cells were treated with PBS+L or PN+L for 24 h. The mRNA levels of Bax, Bcl-2 were assessed using qRT-PCR. **C-D** Cal27 and Tu686 cells were treated with PBS+L or

PN + L for 24 h. The mRNA levels of E-cadherin, N-cadherin and Vimentin were assessed using qRT-PCR. \*\* $p < 0.01$ , \*\*\* $p < 0.001$ . All data are shown as the mean  $\pm$  SD from three independent experiments

**Supplementary Material 3: Figure S2.** Effect of CDDP on HNSCC cells. **A-B** Cal27 and Tu686 cells were treated with H<sub>2</sub>O or CDDP, and the cell cycle was assessed by flow cytometry. **C-D** Cal27 and Tu686 cells were treated with H<sub>2</sub>O or CDDP, and the apoptosis rate was assessed by flow cytometry. **E-F** The migration ability of HNSCC cells was evaluated by scratch assay. Scale bar: 50  $\mu$ m. **G-H** Transwell invasion assay was used to evaluate the invasion ability of HNSCC cells. Scale bar: 50  $\mu$ m. \* $p < 0.05$ , \*\* $p < 0.01$ , \*\*\* $p < 0.001$ , \*\*\*\* $p < 0.0001$ . All data are shown as the mean  $\pm$  SD from three independent experiments

### Acknowledgements

The Fig. 7 in the manuscript were drawn by in Figdraw.

### Author contributions

Qian Lin: Conceptualization, Data curation, Writing – original draft. Hui-Min Liu: Conceptualization, Formal analysis, Project administration. Li-Zhi Wu: Data curation, Investigation, Project administration. Dong-Dong Yu: Methodology, Supervision. Cheng-Yu Hua: Formal analysis, Visualization. You Zou: Methodology, Visualization. Wo-Er Jiao: Methodology, Visualization. Xiang-Pan Li: Conceptualization, Writing – review & editing. Shi-Ming Chen: Conceptualization, Writing – review & editing.

### Funding

This study was supported by the National Natural Science Foundation of China [82371116, 82301274] and supported by the Fundamental Research Funds for the Central Universities of China [Grant No. 2042023kf0013]. The funders had no role in study design, data analysis, preparation of the manuscript, or decision to publish.

### Data availability

All data and materials utilized in the current study are accessible through the corresponding author upon a legitimate request.

### Declarations

#### Ethics approval and consent to participate

The Laboratory Animal Welfare and Ethics Committee of Renmin Hospital of Wuhan University reviewed and approved the animal procedures (Approval No: WDRM20240704B). All animal experiments were conducted following the NIH Guide for the Care and Use of Laboratory Animals (NIH Publication No. 80–23; revised 1978).

#### Consent for publication

All authors have confirmed that all data from this study is publishable and have seen the final version of the article for publication. Written informed consent for publication was obtained from all participants.

#### Competing interests

The authors report no conflicts of interest in this work.

#### Author details

<sup>1</sup>Department of Otolaryngology-Head and Neck Surgery, Renmin Hospital of Wuhan University, 238 Jie-Fang Road, Wuhan, Hubei 430060, P. R. China

<sup>2</sup>Department of Anesthesiology, Renmin Hospital of Wuhan University, No. 238, Jie-Fang Road, Wuhan, Hubei 430060, P. R. China

<sup>3</sup>Department of Oncology, Renmin Hospital of Wuhan University, No. 238, Jie-Fang Road, Wuhan, Hubei 430060, P. R. China

Received: 14 August 2024 / Accepted: 4 November 2024

Published online: 19 November 2024

### References

- Johnson DE, Burtneß B, Leemans CR, Lui WY, Bauman JE, Grandis JR. Head and neck squamous cell carcinoma. *Nat Rev Dis Primers* Nov. 2020;26(11):92. <https://doi.org/10.1038/s41572-020-00224-3>.
- Valero C, Golkaram M, Vos JL, et al. Clinical-genomic determinants of immune checkpoint blockade response in head and neck squamous cell carcinoma. *J Clin Invest* Oct. 2023;2(19). <https://doi.org/10.1172/jci169823>.
- Michaud DS, Langevin SM, Eliot M, et al. High-risk HPV types and head and neck cancer. *Int J Cancer* Oct. 2014;1(7):1653–61. <https://doi.org/10.1002/ijc.28811>.
- Lee NCJ, Kelly JR, Park HS, et al. Patterns of failure in high-metastatic node number human papillomavirus-positive oropharyngeal carcinoma. *Oral Oncol* Oct. 2018;85:35–9. <https://doi.org/10.1016/j.oraloncology.2018.08.001>.
- Adelstein DJ, Li Y, Adams GL, et al. An intergroup phase III comparison of standard radiation therapy and two schedules of concurrent chemoradiotherapy in patients with unresectable squamous cell head and neck cancer. *J Clin Oncol* Jan. 2003;1(1):92–8. <https://doi.org/10.1200/jco.2003.01.008>.
- Seiwert TY, Burtneß B, Mehra R, et al. Safety and clinical activity of pembrolizumab for treatment of recurrent or metastatic squamous cell carcinoma of the head and neck (KEYNOTE-012): an open-label, multicentre, phase 1b trial. *Lancet Oncol* Jul. 2016;17(7):956–65. [https://doi.org/10.1016/s1470-2045\(16\)30066-3](https://doi.org/10.1016/s1470-2045(16)30066-3).
- Oliva M, Spreafico A, Taberna M, et al. Immune biomarkers of response to immune-checkpoint inhibitors in head and neck squamous cell carcinoma. *Ann Oncol* Jan. 2019;1(1):57–67. <https://doi.org/10.1093/annonc/mdy507>.
- Haddad RI, Shin DM. Recent advances in head and neck cancer. *N Engl J Med* Sep. 2008;1(11):1143–54. <https://doi.org/10.1056/NEJMra0707975>.
- Yang Z, Chen X. Semiconducting perylene Diimide Nanostructure: multifunctional phototheranostic nanoplatform. *Acc Chem Res* May. 2019;21(5):1245–54. <https://doi.org/10.1021/acs.accounts.9b00064>.
- Gao J, Wang F, Wang S, et al. Hyperthermia-triggered On-Demand Biomimetic Nanocarriers for Synergetic Photothermal and Chemotherapy. *Adv Sci (Weinh)* Jun. 2020;7(11):1903642. <https://doi.org/10.1002/adv.201903642>.
- Vankayala R, Hwang KC. Near-Infrared-Light-Activatable nanomaterial-mediated phototheranostic nanomedicines: an emerging paradigm for Cancer Treatment. *Adv Mater* Jun. 2018;30(23):e1706320. <https://doi.org/10.1002/adma.201706320>.
- Denkova AG, de Kruijff RM, Serra-Crespo P. Nanocarrier-mediated photochemotherapy and Photoradiotherapy. *Adv Healthc Mater* Apr. 2018;7(8):e1701211. <https://doi.org/10.1002/adhm.201701211>.
- Cheng Z, Li M, Dey R, Chen Y. Nanomaterials for cancer therapy: current progress and perspectives. *J Hematol Oncol* May. 2021;31(1):85. <https://doi.org/10.1186/s13045-021-01096-0>.
- Ning S, Lyu M, Zhu D, et al. Type-I AIE photosensitizer loaded Biomimetic System boosting cuproptosis to inhibit breast Cancer Metastasis and Recurrence. *ACS Nano* Jun. 2023;13(11):10206–17. <https://doi.org/10.1021/acsnano.3c00326>.
- Chakravarty S, Roy Chowdhury S, Mukherjee S. AIE materials for cancer cell detection, bioimaging and theranostics. *Prog Mol Biol Transl Sci*. 2021;185:19–44. <https://doi.org/10.1016/bs.pmbts.2021.07.032>.
- Li J, Wang J, Li H, Song N, Wang D, Tang BZ. Supramolecular materials based on AIE luminogens (AIEgens): construction and applications. *Chem Soc Rev* Feb. 2020;24(4):1144–72. <https://doi.org/10.1039/c9cs00495e>.
- Cui M, Tang D, Wang B, Zhang H, Liang G, Xiao H. Bioorthogonal guided activation of cGAS-STING by AIE Photosensitizer nanoparticles for targeted tumor therapy and imaging. *Adv Mater* Dec. 2023;35(52):e2305668. <https://doi.org/10.1002/adma.202305668>.
- Hammouda MB, Ford AE, Liu Y, Zhang JY. The JNK Signaling Pathway in inflammatory skin disorders and Cancer. *Cells* Apr. 2020;2(4). <https://doi.org/10.3390/cells9040857>.
- Weston CR, Davis RJ. The JNK signal transduction pathway. *Curr Opin Cell Biol* Apr. 2007;19(2):142–9. <https://doi.org/10.1016/j.ceb.2007.02.001>.
- Bogoyevitch MA, Kobe B. Uses for JNK: the many and varied substrates of the c-Jun N-terminal kinases. *Microbiol Mol Biol Rev* Dec. 2006;70(4):1061–95. <https://doi.org/10.1128/mmr.00025-06>.
- Zhang N, Peng F, Wang Y, et al. Shikonin induces colorectal carcinoma cells apoptosis and autophagy by targeting galectin-1/JNK signaling axis. *Int J Biol Sci*. 2020;16(1):147–61. <https://doi.org/10.7150/ijbs.36955>.

22. Wang F, Wu P, Qin S, et al. Curcumin inhibits osteosarcoma cell line U2OS proliferation by ROS induced apoptosis, autophagy and cell cycle arrest through activating JNK signaling pathway. *Int J Biol Macromol* Jan. 2022;151:195:433–9. <https://doi.org/10.1016/j.jbiomac.2021.11.156>.
23. Yang J, Li ZD, Hou CY, et al. EM-2 inhibited autophagy and promoted G(2)/M phase arrest and apoptosis by activating the JNK pathway in hepatocellular carcinoma cells. *Acta Pharmacol Sin* Jul. 2021;42(7):1139–49. <https://doi.org/10.1038/s41401-020-00564-6>.
24. Wu H, Guo H, Liu H, et al. Copper sulfate-induced endoplasmic reticulum stress promotes hepatic apoptosis by activating CHOP, JNK and caspase-12 signaling pathways. *Ecotoxicol Environ Saf Mar*. 2020;151:191:110236. <https://doi.org/10.1016/j.ecoenv.2020.110236>.
25. Dhanasekaran DN, Reddy EP. JNK signaling in apoptosis. *Oncogene* Oct. 2008;20(48):6245–51. <https://doi.org/10.1038/ncr.2008.301>.
26. Sun Y, Zhang D, Guo X, et al. MKK3 modulates JNK-dependent cell migration and invasion. *Cell Death Dis* Feb. 2019;15(3):149. <https://doi.org/10.1038/s41419-019-1350-6>.
27. Zhang L, Wang Z, Zhang R, et al. Multi-stimuli-responsive and cell membrane camouflaged Aggregation-Induced Emission Nanogels for Precise Chemo-Photothermal synergistic therapy of tumors. *ACS Nano* Dec. 2023;26(24):25205–21. <https://doi.org/10.1021/acsnano.3c08409>.
28. Gao D, Lo PC. Polymeric micelles encapsulating pH-responsive doxorubicin prodrug and glutathione-activated zinc(II) phthalocyanine for combined chemotherapy and photodynamic therapy. *J Control Release* Jul. 2018;282:282:46–61. <https://doi.org/10.1016/j.jconrel.2018.04.030>.
29. Kang JI, Choi YK, Han SC, et al. 5-Bromo-3,4-dihydroxybenzaldehyde promotes hair growth through activation of Wnt/ $\beta$ -Catenin and Autophagy Pathways and inhibition of TGF- $\beta$  pathways in dermal papilla cells. *Molecules* Mar. 2022;28(7). <https://doi.org/10.3390/molecules27072176>.
30. Wagner EF, Nebreda AR. Signal integration by JNK and p38 MAPK pathways in cancer development. *Nat Rev Cancer* Aug. 2009;9(8):537–49. <https://doi.org/10.1038/nrc2694>.
31. Solomon B, Young RJ, Rischin D. Head and neck squamous cell carcinoma: Genomics and emerging biomarkers for immunomodulatory cancer treatments. *Semin Cancer Biol* Oct. 2018;52(Pt 2):228–40. <https://doi.org/10.1016/j.semcancer.2018.01.008>.
32. Kitamura N, Sento S, Yoshizawa Y, Sasabe E, Kudo Y, Yamamoto T. Current trends and future prospects of molecular targeted therapy in Head and Neck squamous cell carcinoma. *Int J Mol Sci* Dec. 2020;29(1). <https://doi.org/10.3390/ijms22010240>.
33. Chen Q, Liang C, Wang C, Liu Z. An imagable and photothermal abraxane-like nanodrug for combination cancer therapy to treat subcutaneous and metastatic breast tumors. *Adv Mater* Feb. 2015;4(5):903–10. <https://doi.org/10.1002/adma.201404308>.
34. Wang X, Gu Y, Li Q, et al. Synergistic chemo-photothermal cancer therapy of pH-responsive polymeric nanoparticles loaded IR825 and DTX with charge-reversal property. *Colloids Surf B Biointerfaces* Jan. 2022;209(Pt 2):112164. <https://doi.org/10.1016/j.colsurfb.2021.112164>.
35. Zhu C, Kwok RTK, Lam JWY, Tang BZ. Aggregation-Induced Emission. A trailblazing journey to the field of Biomedicine. *ACS Appl Bio Mater* Dec. 2018;17(6):1768–86. <https://doi.org/10.1021/acsbm.8b00600>.
36. Zhao Z, Tang BZ. AIE study: a stepping stone to aggregate science. *Natl Sci Rev* Jun. 2021;8(6):nwab079. <https://doi.org/10.1093/nsr/nwab079>.
37. Singh R, Letai A, Sarosiek K. Regulation of apoptosis in health and disease: the balancing act of BCL-2 family proteins. *Nat Rev Mol Cell Biol* Mar. 2019;20(3):175–93. <https://doi.org/10.1038/s41580-018-0089-8>.
38. Spitz AZ, Gavathiotis E. Physiological and pharmacological modulation of BAX. *Trends Pharmacol Sci Mar*. 2022;43(3):206–20. <https://doi.org/10.1016/j.tips.2021.11.001>.
39. Spitz AZ, Zacharioudakis E, Reyna DE, Garner TP, Gavathiotis E. Eltrombopag directly inhibits BAX and prevents cell death. *Nat Commun* Feb. 2021;18(1):1134. <https://doi.org/10.1038/s41467-021-21224-1>.
40. Pastushenko I, Blanpain C. EMT Transition States during Tumor Progression and Metastasis. *Trends Cell Biol* Mar. 2019;29(3):212–26. <https://doi.org/10.1016/j.tcb.2018.12.001>.
41. Thiery JP. Epithelial-mesenchymal transitions in tumour progression. *Nat Rev Cancer* Jun. 2002;2(6):442–54. <https://doi.org/10.1038/nrc822>.
42. Green KJ, Gaudry CA. Are desmosomes more than tethers for intermediate filaments? *Nat Rev Mol Cell Biol* Dec. 2000;1(3):208–16. <https://doi.org/10.1038/35043032>.
43. Lv M, Zhong Z, Huang M, Tian Q, Jiang R, Chen J. lncRNA H19 regulates epithelial-mesenchymal transition and metastasis of bladder cancer by miR-29b-3p as competing endogenous RNA. *Biochim Biophys Acta Mol Cell Res* Oct. 2017;1864(10):1887–99. <https://doi.org/10.1016/j.bbamcr.2017.08.001>.
44. Yan H, He L, Lv D, Yang J, Yuan Z. The role of the dysregulated JNK Signaling Pathway in the Pathogenesis of Human diseases and its potential therapeutic strategies: a Comprehensive Review. *Biomolecules* Feb. 2024;19(2). <https://doi.org/10.3390/biom14020243>.
45. Lee E, Han AR, Nam B, et al. Moscatilin induces apoptosis in Human Head and Neck Squamous Cell Carcinoma Cells via JNK Signaling Pathway. *Molecules* Feb. 2020;25(4). <https://doi.org/10.3390/molecules25040901>.
46. Ho HY, Lin CC, Chuang YC, Lo YS, Hsieh MJ, Chen MK. Apoptotic effects of dehydrocristadine via JNK and ERK pathway regulation in oral squamous cell carcinoma. *Biomed Pharmacother* May. 2021;137:111362. <https://doi.org/10.1016/j.biopha.2021.111362>.
47. Low HB, Wong ZL, Wu B, et al. DUSP16 promotes cancer chemoresistance through regulation of mitochondria-mediated cell death. *Nat Commun* Apr. 2021;16(1):2284. <https://doi.org/10.1038/s41467-021-22638-7>.
48. Görögh T, Bèress L, Quabius ES, Ambrosch P, Hoffmann M. Head and neck cancer cells and xenografts are very sensitive to palytoxin: decrease of c-jun n-terminale kinase-3 expression enhances palytoxin toxicity. *Mol Cancer* Feb. 2013;14:12:12. <https://doi.org/10.1186/1476-4598-12-12>.

## Publisher's note

Springer Nature remains neutral with regard to jurisdictional claims in published maps and institutional affiliations.